AIAA JOURNAL
Vol. 42, No. 10, October 2004

Numerical Simulation of Fore and Aft Sound Fields of a Turbofan

Y. Özyörük*
Middle East Technical University, 06531 Ankara, Turkey
and
V. Ahuja†
Combustion Research and Flow Technology, Inc., Pipersville, Pennsylvania 18947

A framework for predicting fan related noise from high bypass ratio engines is presented. The methodology accounts for both fore and aft radiation and includes the effects of liner treatment on the engine walls. Solutions are obtained through a combination of Euler and linearized Euler solvers, coupled with a Kirchhoff formulation for far-field noise prediction. The nacelle region is solved using the Euler solver, whereas the linearized Euler solver is used for the fan exhaust stage. Switching to the linearized Euler solver in the aft region has been necessary to overcome difficulties experienced due to the coupling of the acoustic modes with flow near the engine exhaust boundary and appearance of flow instabilities in the shear layer trailing the exhaust shroud. Results are presented for spinning modes from a turbofan engine with acoustic treatment.

Nomenclature

A	=	modal amplitude of acoustic pressure; cross-sectional area
a, b	=	constants in z-domain impedance model
B	=	number of fan blades
c	=	speed of sound
e	=	energy per unit volume
i	=	$\sqrt{-1}$
J, Y	=	Bessel functions of the first and second kind, respectively
M	=	Mach number
m	=	azimuthal mode number
$\dot{m}$	=	mass flow rate
n	=	time harmonic index
$\boldsymbol{n}$	=	surface unit normal vector
p	=	pressure
$\hat{p}$	=	complex amplitude of pressure perturbation
R_{bp}	=	bypass ratio
R_{fc}	=	fan compression ratio
R_{wc}	=	radius of wall curvature
r	=	radial coordinate; radius
S	=	Kirchhoff surface area
s	=	integer number
T	=	temperature
t	=	time
u, v, w	=	axial, radial, and azimuthal velocity components, respectively
V	=	number of vanes; velocity magnitude
$\boldsymbol{V}$	=	total velocity vector
$\hat{v}$	=	complex amplitude of velocity perturbation
(x, r, θ)	=	cylindrical polar coordinates
(x, y, z)	=	cartesian coordinates
$\boldsymbol{x}$	=	spatial coordinate; observer coordinate
$\boldsymbol{y}$	=	Kirchhoff surface coordinate
Z	=	impedance
z	=	complex variable
γ	=	ratio of specific heats
Δt	=	time increment
θ	=	azimuthal angle
μ	=	radial mode order
(ξ, η, ζ)	=	curvilinear coordinates
ρ	=	density
σ	=	hub-to-tip ratio
τ	=	surface emission (retarded) time
ϕ	=	phase of acoustic mode
φ	=	angle between surface normal and radiation direction
ω	=	angular frequency

Subscripts

a	=	flow perturbation
C	=	contravariant
ex	=	exhaust fan-face
in	=	inlet fan-face
n	=	normal component to surface
t	=	tangential component to surface
tip	=	rotor blade tip
0	=	mean value
∞	=	freestream value

Superscript

n	=	time step

Received 13 August 2002; revision received 23 September 2003; accepted for publication 4 March 2004.

*Associate Professor, Department of Aerospace Engineering; ozyoruk@metu.edu.tr.

†Research Scientist; vineet@craft-tech.com. Senior Member AIAA.

I. Introduction

STRICT controls for jet noise reduction have led to increased emphasis on fan-generated thrust in high bypass ratio engines that have become commonplace in commercial air travel. However, fan noise has become a significant source of sound, especially for communities close to airports. The analysis of fan noise is challenging because it is a multifaceted problem that requires 1) identification of the spinning modes due to the rotor and the interaction between the rotor and the downstream stator, 2) propagation of these modes in the engine ducting, 3) analysis of the impact of lining material in damping these modes, and 4) propagation of the resultant sound to the far field accounting for aerodynamic acoustic coupling and wave refraction. In the past, it has been difficult to perform a full analysis of the entire engine, and a piecemeal strategy was adopted to understand the issues relevant to each of the individual components of the engine fan noise problem. Tyler and Sofrin[1] analytically identified and classified the noise-generating mechanisms in axial flow turbomachinery systems. In recent years, Rumsey et al.[2] have

used a Navier–Stokes approach to look at acoustic modes emanating from rotor–wake stator–blade interaction. Analysis of mode propagation in the engine nacelle and aft duct is important primarily to identify the cut-on modes and study the effects of flow disturbances/perturbations (boundary layer, turbulence, etc.) on these modes.[3,4] The complexity of solving the far-field engine noise problem in itself precluded researchers, until very recently, from including effects due to the acoustic treatment of engine walls. For the most part, liner research evolved independently (through the use of empirical models) from computational aeroacoustics-based methods for predicting engine noise. Sophisticated liner materials are now used as effective damping mechanisms and can potentially be tuned to attenuate noise over a range of frequencies.[5] Significant work has been done for prediction of sound radiating from engine inlets using hard-wall boundary conditions by many research groups.[6–11] However, most of these prediction methods preclude capturing of second-order effects such as aerodynamic–acoustic coupling, wave refraction, etc. This shortcoming has been overcome by the authors in the past[12] by the utilization of a combined Euler equations–Kirchhoff formulation to evaluate far-field noise.

However, most of this work was limited to engine nacelles. Including aft radiation from the engine exhaust in these analyses raises issues related to grid topologies, convergence, unsteady numerics, and boundary conditions. Most of these issues were dealt with by the authors in Ref. 13. However, the comparisons made in that paper were limited to radiation without mass flow, for example, dipole in a cylinder simulating an engine with acoustic modes, engine with centerbody, etc. When mass flow exists, the conditions applied at the inflow boundary of the exhaust (Fig. 1) require special attention in numerical simulations. Ideally these conditions must function to introduce acoustic waves of desired frequencies and modal shapes into the domain and, at the same time, permit the outgoing waves without reflection. The boundary conditions must also yield the desired operating conditions, for example, mass flow rate through the exhaust, in computation of the mean flow over which acoustic perturbations are introduced. Nonreflective property is generally attained through appropriate sets of equations based on the characteristics of the flow normal to the boundary.[14–16] Alternative methods such as buffer zones and perfectly matched layers[17,18] have also been proposed recently as dampers of outgoing waves, but all of these increase the computational cost. Giles[16] gave characteristics-based, well-posed nonreflecting boundary conditions for the solution of two-dimensional, linearized Euler equations. When these conditions were modified and extended to three dimensions for full Euler computations of the exhaust acoustic field, they behaved poorly and resulted in exponentially growing waves. Interestingly though, when the extended boundary conditions were used, a converged mean flow could be obtained, but somewhat at a different operating condition than that specified.[19] In addition, when the linearized Euler equations and the extended inflow boundary conditions were coupled, it was possible to perform successful acoustic computations. Note that such a difficulty did not arise at the outflow boundary of the engine inlet (Fig. 1) with the full Euler equations. This is primarily because of the larger number of characteristics that enter the computational domain from an inflow boundary than an outflow boundary. At the former, attention must also be given to the entropy and vorticity waves, complicating the boundary conditions further, especially with nonuniform inflow.

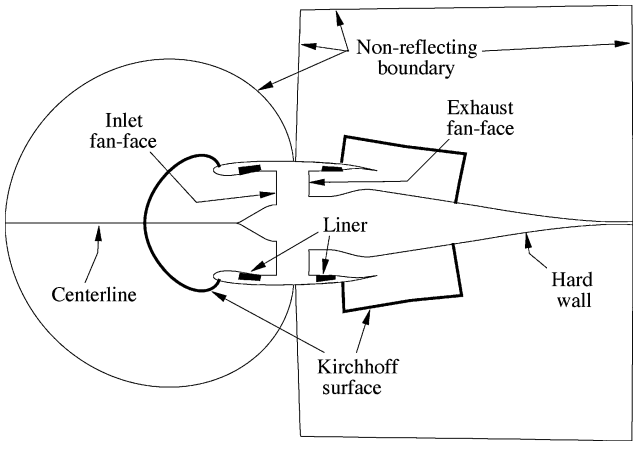

Fig. 1 Schematic of solution domain and its boundaries.

Another very important issue in full Euler solutions of the engine exhaust is related to shear layer instabilities. These instabilities appear in long-time computations of the exhaust flowfield on meshes that are designed to resolve the acoustic modes.[19] Although such flow instabilities are also supported by the linearized Euler equations, they are confined only to near field[20] and are observed in longer times. Therefore, in the present work, to prevent the appearance of such instabilities early and to circumvent the difficulties in coupling the exhaust inflow boundary conditions and the full Euler equations, the linearized Euler equations are employed as the governing equations in prediction of the aft fan noise.

In this paper, the authors present a framework for predicting fan noise from a full engine configuration taking into account the effects of acoustic treatment on the engine walls. The framework used in this paper, extends the previous work of the authors of predicting far-field noise from engine nacelles. The noise-generating mechanisms are based on the theory of Tyler and Sofrin[1] and are not computed directly but explicitly prescribed as sources. Furthermore, the compressor exhaust is eliminated by carrying the aft end of the centerbody all of the way to the axis of symmetry. The focus is on fan noise, and jet noise is beyond the scope of the paper. The lining on the engine walls is modeled as a z-transform-based impedance condition directly in the time-domain computations.[21,22] Note that even though data comparisons for the fan noise radiation from the full engine configuration is difficult because of lack of experimental data in the open literature, the entire framework presented in this paper has been validated in all its stages of development. For example, the full Euler–Kirchhoff formulation has been shown to predict sound adequately for the JT15D engine inlet and has compared favorably with semi-analytical methods[22,23]; the impedance condition has been extensively tested against data from NASA Langley Research Center flow impedance tube.[21]

The paper is organized as follows: in the next section details of the computational framework are discussed: the governing equations, the boundary conditions, and the impedance condition. This is followed by simulations of fore and aft radiation from a full engine configuration. Our interest is in evaluating spinning modes emanating from the engine rotor–stator system, and our simulations demonstrate the effectiveness of our framework in prediction of far-field noise. We close the paper with our observations regarding difficulties observed during the course of the simulations and some concluding remarks.

II. Governing Equations

As indicated earlier, the problem of propagation and radiation is solved using a full Euler solver in the inlet part and a linearized Euler solver in the exhaust part of the engine. Solving the full Euler equations, instead of the linearized Euler equations, for the inlet increases the computational cost only slightly. Therefore, the Euler equations are employed for prediction of fore radiation, which is dominated by the inlet acoustic field.

A. Euler Equations

The governing equations of the full Euler solver are the three-dimensional, time-dependent, conservative form of the Euler equations, which are given in cylindrical-polar coordinates as

$$\frac{\partial \boldsymbol{Q}}{\partial t} + \frac{\partial \boldsymbol{E}}{\partial x} + \frac{\partial \boldsymbol{F}}{\partial r} + \frac{1}{r}\frac{\partial \boldsymbol{G}}{\partial \theta} + \frac{\boldsymbol{H}}{\boldsymbol{r}} = 0 \tag{1}$$

where $\boldsymbol{Q}$ is the conservative solution vector, $\boldsymbol{E}$, $\boldsymbol{F}$, and $\boldsymbol{G}$ are the vector components of the flux tensor, and $\boldsymbol{H}$ is the source term due formulation in cylindrical-polar coordinates. These terms are

given as

$$\boldsymbol{Q}=\begin{Bmatrix}\rho\\ \rho u\\ \rho v\\ \rho w\\ \rho e\end{Bmatrix},\qquad \boldsymbol{E}=\begin{Bmatrix}\rho u\\ \rho u^2+p\\ \rho uv\\ \rho uw\\ (\rho e+p)u\end{Bmatrix},\qquad \boldsymbol{F}=\begin{Bmatrix}\rho v\\ \rho vu\\ \rho v^2+p\\ \rho vw\\ (\rho e+p)v\end{Bmatrix}$$

$$\boldsymbol{G}=\begin{Bmatrix}\rho w\\ \rho wu\\ \rho wv\\ \rho w^2+p\\ (\rho e+p)w\end{Bmatrix},\qquad \boldsymbol{H}=\begin{Bmatrix}\rho v\\ \rho vu\\ \rho v^2-\rho w^2\\ 2\rho vw\\ (\rho e+p)v\end{Bmatrix} \tag{2}$$

the energy per unit volume is found from the equation of state given by

$$\rho e=p/(\gamma-1)+\tfrac{1}{2}\rho(u^2+v^2+w^2) \tag{3}$$

B. Linearized Euler Equations

The governing equations of the linearized Euler solver are obtained by linearizing the primitive form of the three-dimensional, time-dependent Euler equations about an axisymmetric, nonuniform mean flow. The linearized equations are given in cylindrical-polar coordinates as

$$\frac{\partial u_a}{\partial t}+u_0\frac{\partial u_a}{\partial x}+v_0\frac{\partial u_a}{\partial r}+u_a\frac{\partial u_0}{\partial x}+v_a\frac{\partial u_0}{\partial r}+\frac{1}{\rho_0}\frac{\partial p_a}{\partial x}-\frac{p_a}{\rho_0^2c_0^2}\frac{\partial p_0}{\partial x}=0 \tag{4}$$

$$\frac{\partial v_a}{\partial t}+u_0\frac{\partial v_a}{\partial x}+v_0\frac{\partial v_a}{\partial r}+u_a\frac{\partial v_0}{\partial x}+v_a\frac{\partial v_0}{\partial r}+\frac{1}{\rho_0}\frac{\partial p_a}{\partial r}-\frac{p_a}{\rho_0^2c_0^2}\frac{\partial p_0}{\partial r}=0 \tag{5}$$

$$\frac{\partial w_a}{\partial t}+u_0\frac{\partial w_a}{\partial x}+v_0\frac{\partial w_a}{\partial r}+\frac{1}{\rho_0 r}\frac{\partial p_a}{\partial \theta}+\frac{v_0w_a}{r}=0 \tag{6}$$

$$\frac{\partial p_a}{\partial t}+u_0\frac{\partial p_a}{\partial x}+v_0\frac{\partial p_a}{\partial r}+u_a\frac{\partial p_0}{\partial x}+v_a\frac{\partial p_0}{\partial r}+\gamma p_0\left(\frac{\partial u_a}{\partial x}+\frac{\partial v_a}{\partial r}+\frac{v_a}{r}+\frac{1}{r}\frac{\partial w_a}{\partial \theta}\right)+\gamma p_a\left(\frac{\partial u_0}{\partial x}+\frac{\partial v_0}{\partial r}+\frac{v_0}{r}\right)=0 \tag{7}$$

C. Boundary Conditions

1. Fan-Face Conditions

Acoustic source conditions at inlet fan-face. Exact cylindrical duct eigensolutions are used in definition of the acoustic source at upstream and downstream faces of the fan rotor–stator stage, which will be called hereafter as the inlet fan-face and exhaust fan-face (Fig. 1), respectively. Acoustic pressure at a cross section in an annular duct is given in cylindrical-polar coordinates as

$$p_a(r,\theta,t)=\Re\sum_m\sum_\mu A_{m\mu}[J_m(k_{m\mu}r)+Q_{m\mu}Y_m(k_{m\mu}r)]\times\exp[i(\omega t+m\theta+\phi_{m\mu})] \tag{8}$$

where the eigenvalues $k_{m\mu}$ are found by solving the equation resulting from the wall condition, that is, $\partial p_a/\partial r|_{\text{wall}}=0$. Then, $Q_{m\mu}=-J'_m(\sigma k_{m\mu}r_{\text{tip}})/Y'_m(\sigma k_{m\mu}r_{\text{tip}})$ with J' and Y' being the derivatives of J and Y with respect to r, respectively. When there is no centerbody, that is, $\sigma=0$, $Q_{m\mu}$ is zero. The azimuthal mode order m is found using the rotor–stator interaction theory of Tyler and Sofrin.[1] According to this theory, $m=nB+sV$. The number of rotor blades, number of exit guide vanes and the rotor speed are entered as part of the input for the solver, and the modes that are cut on are automatically determined based on the local mean flow conditions at the inlet and exhaust fan-faces. Multiple harmonics of the fundamental frequency (blade passing frequency) are often seen in turbomachinery acoustics. When a multifrequency analysis is required, a summation is performed over all of the relevant frequencies that comprise the source.

At the inlet fan-face, acoustic pressure given by Eq. (8) is specified as a perturbation to the mean pressure, and the other variables are solved using the interior equations. This approach works sufficiently well when the cutoff ratios for the inlet modes are away from unity.

Acoustic source conditions at exhaust fan-face. At the exhaust fan-face we apply a different approach. The conditions applied at the exhaust fan-face stem from the characteristics-based inflow conditions of Giles.[16] These conditions are modified and extended to three dimensions and are given in cylindrical-polar coordinates as

$$\frac{\partial u_a}{\partial t}+\frac{c_0-u_0}{2\rho_0c_0}\left[\frac{\partial p_a}{\partial x}-\rho_0c_0\frac{\partial u_a}{\partial x}\right]-\frac{u_0+c_0}{4}\left[\frac{\partial v_a}{\partial r}+\frac{v_a}{r}\right]-\frac{u_0+c_0}{4r}\frac{\partial w_a}{\partial \theta}=-v_a\frac{\partial u_0}{\partial r}-\frac{\mathcal{L}_5}{2\rho_0c_0} \tag{9}$$

$$\frac{\partial v_a}{\partial t}+u_0\frac{\partial v_a}{\partial r}+\frac{1}{\rho_0}\frac{\partial p_a}{\partial r}=0 \tag{10}$$

$$\frac{\partial w_a}{\partial t}+\frac{u_0}{r}\frac{\partial w_a}{\partial \theta}+\frac{1}{\rho_0 r}\frac{\partial p_a}{\partial \theta}=0 \tag{11}$$

$$\frac{\partial p_a}{\partial t}+\frac{u_0-c_0}{2}\left[\frac{\partial p_a}{\partial x}-\rho_0c_0\frac{\partial u_a}{\partial x}\right]+\frac{3c_0-u_0}{4}\rho_0c_0\left[\frac{\partial v_a}{\partial r}+\frac{v_a}{r}\right]+\frac{3c_0-u_0}{4r}\rho_0c_0\frac{\partial w_a}{\partial \theta}=-\frac{\mathcal{L}_5}{2} \tag{12}$$

where $\mathcal{L}_5$ is set such that these boundary conditions yield a similar acoustic excitation to that dictated by Eq. (8).

Mean flow conditions at inlet fan-face. Mean flow calculations, however, employ a simpler, one-dimensional version of the characteristics-based boundary conditions at both the inlet and exhaust fan-faces. First, the inlet fan-face mean flow quantities are determined analytically using the total mass flow rate through the inlet, freestream Mach number, inlet fan-face cross-sectional area information and ideal one-dimensional gasdynamics relations. The mean Mach number at the inlet fan-face is obtained by solving the equation

$$\frac{\dot m}{\rho_\infty c_\infty}A_{\text{in}}=M_{0,\text{in}}\left[\frac{1+[(\gamma-1)/2]M_\infty^2}{1+[(\gamma-1)/2]M_{0,\text{in}}^2}\right]^{(\gamma+1)/2(\gamma-1)} \tag{13}$$

Then the mean density, pressure, and speed of sound are found using the relations

$$\frac{T_{0,\text{in}}}{T_\infty}=\frac{1+[(\gamma-1)/2]M_\infty^2}{1+[(\gamma-1)/2]M_{0,\text{in}}^2} \tag{14}$$

$$\rho_{0,\text{in}}=\rho_\infty(T_{0,\text{in}}/T_\infty)^{1/(\gamma-1)} \tag{15}$$

$$p_{0,\text{in}}=p_\infty(T_{0,\text{in}}/T_\infty)^{\gamma/(\gamma-1)} \tag{16}$$

$$c_{0,\text{in}}=(\gamma p_{0,\text{in}}/\rho_{0,\text{in}})^{\frac{1}{2}} \tag{17}$$

In the iteration of the solution to steady state, the mean pressure given by the preceding relations is used in the one-dimensional characteristic equation given for the inlet fan-face as

$$p=p_{0,\text{in}}+\rho_{0,\text{in}}c_{0,\text{in}}(u-M_{0,\text{in}}c_{0,\text{in}}) \tag{18}$$

The other flow variables are solved at the inlet fan-face using the interior equations. This procedure yields very accurate numerical mass flow rates.

Mean flow conditions at exhaust fan-face. The exhaust fan-face mean quantities are determined based on the inlet fan-face conditions, bypass ratio, fan compression ratio, exhaust fan-face area information and assumption that the Mach number across the fan rotor–stator stage is constant. Based on the operating conditions, target mean quantities are defined first for the exhaust fan-face as follows:

$$c_{0,\mathrm{ex}} = \gamma R_{\mathrm{fc}}\, p_{0,\mathrm{in}} M_{0,\mathrm{in}} A_{\mathrm{ex}}(1 + R_{\mathrm{bp}})/\dot{m} R_{\mathrm{bp}} \tag{19}$$

$$p_{0,\mathrm{ex}} = R_{\mathrm{fc}}\, p_{0,\mathrm{in}} \tag{20}$$

$$\rho_{0,\mathrm{ex}} = \gamma p_{0,\mathrm{ex}} \big/ c_{0,\mathrm{ex}}^2 \tag{21}$$

Then, to obtain the exhaust background flowfield through the Euler solver, these mean quantities are used at the boundary in the following manner:

$$\rho u = \dot{m} R_{\mathrm{bp}} / A_{\mathrm{ex}} \tag{22}$$

$$\rho v = 0 \tag{23}$$

$$\rho w = 0 \tag{24}$$

$$p = p_{0,\mathrm{ex}} - \rho_{0,\mathrm{ex}} c_{0,\mathrm{ex}} (u - M_{0,\mathrm{ex}} c_{0,\mathrm{ex}}) \tag{25}$$

An attempt to evaluate the density directly from Eq. (21) resulted in divergent solutions, and therefore, the density is obtained at the boundary solving the continuity equation. This boundary condition procedure resulted in converged exhaust flows with nearly uniform but somewhat lower fan-face pressure and density than their target values. However, when the three-dimensional characteristics-based boundary conditions given by Eqs. (9–12) were directly coupled to the Euler equations and used in the mean flow computations, the converged mean flow quantities exhibited to some extent radial variations, in addition to some differences from the target values. Such variations and differences made the acoustic computations using the full Euler solver in conjunction with the boundary conditions given by Eqs. (9–12) ill behaved, resulting in growing waves at the exhaust fan-face. Therefore, we had to resort to the preceding simpler boundary conditions, Eqs. (22–25), for successful computations of the exhaust mean flow and to the boundary conditions given by Eqs. (9–12) coupled with the linearized Euler equations for successful computations of the exhaust acoustic field.

2. Hard-Wall Conditions

Slip-wall conditions are applied over a hard wall in both Euler and linearized Euler computations. The physical domain is transformed into body-fitted coordinates through the mappings

$$x = x(\xi, \eta), \qquad r = r(\xi, \eta), \qquad \theta = \theta(\zeta) \tag{26}$$

Then the contravariant velocities are written as

$$u_C = \xi_x u + \xi_r v + (\xi_\theta / r) w \tag{27}$$

$$v_C = \eta_x u + \eta_r v + (\eta_\theta / r) w \tag{28}$$

$$w_C = \zeta_x u + \zeta_r v + (\zeta_\theta / r) w \tag{29}$$

where $\partial(\xi, \eta, \zeta)/\partial(x, r, \theta)$ are the transformation metrics.[23] Numerically the normal contravariant velocity v_C is set to zero (where η grid lines are normal to surface) on the wall, and the tangential contravariant velocity components u_C and w_C are extrapolated from the interior solution. Density is also extrapolated from the interior points. Pressure is then found from the normal momentum balance at the wall:

$$\frac{\partial p}{\partial \eta} = \left[\eta_x^2 + \eta_r^2 + \left(\frac{\eta_\theta}{r} \right)^2 \right]^{-\frac{1}{2}} \frac{\rho V_t^2}{R_{\mathrm{wc}}} \tag{30}$$

In the linearized Euler solutions, the preceding equations are simply linearized and applied at a hard wall in the manner outlined earlier.

3. Impedance Condition

The standard impedance condition[24] is applied on acoustically treated surfaces, namely, liners (Fig. 1). Because fluid particles penetrate such surfaces, the same momentum equations as the interior are solved on them, but the energy equation is replaced with the standard, frequency-dependent impedance condition, which is written as

$$i\omega \hat{p}(\boldsymbol{x}, \omega) + \boldsymbol{V}_0 \cdot \nabla \hat{p}(\boldsymbol{x}, \omega) - \boldsymbol{n} \cdot [\boldsymbol{n} \cdot \nabla \boldsymbol{V}_0]\, \hat{p}(\boldsymbol{x}, \omega) = -i\omega Z(\omega) \hat{v}_n(\boldsymbol{x}, \omega) \tag{31}$$

A time-discrete form of this condition is obtained through a sequence of transforms. First, a z transform is applied to convert the impedance condition to a z-domain equivalent.[21] This is done simply by replacing the $i\omega$ term in Eq. (31) with $(1 - z^{-1})/\Delta t$ and writing the complex-dependent variables as functions of z. The resulting equation is then transformed to the time domain by replacing the $(1 - z^{-1})/\Delta t$ term with the time-discretization operator $(\delta^0 - \delta^{-1})/\Delta t$, where δ^m is the discrete shift operator defined as $\delta^m Q^n = Q^{n+m}$. Applying these transformations to the standard impedance condition yields the following time-discrete equivalent:

$$\left(p_a^{n+1} - p_a^n\right)\big/\Delta t + \mathcal{L}_0 p_a^{n+1} = -a_0 \left[\left(v_{a,n}^{n+1} - v_{a,n}^n\right)\big/\Delta t \right] - R_a^n \tag{32}$$

where $\mathcal{L}_0$ is the spatial operator given by $\mathcal{L}_0 = \boldsymbol{V}_0 \cdot \nabla - \boldsymbol{n} \cdot (\boldsymbol{n} \cdot \nabla \boldsymbol{V}_0)$ and

$$R_a^n = \sum_{\ell=1}^{M_N} a_\ell \left[\frac{v_{a,n}^{n+1-\ell} - v_{a,n}^{n-\ell}}{\Delta t} \right] - \sum_{k=1}^{M_D} b_k \left[\frac{p_a^{n+1-k} - p_a^{n-k}}{\Delta t} + \mathcal{L}_0 p_a^{n+1-k} \right] \tag{33}$$

The constant parameters $a_{0,1,\ldots,M_D}$ and $b_{1,\ldots,M_N}$ are found from the z-domain fit of the frequency-dependent impedance, assuming it is given by

$$Z(z) = \frac{a_0 + \sum_{\ell=1}^{M_N} a_\ell z^{-\ell}}{1 - \sum_{k=1}^{M_D} b_k z^{-k}} \tag{34}$$

The coupling of the time-discrete impedance condition with the time-integration algorithm of the governing equations is described in detail in Ref. 22.

4. Far-Field Boundary Conditions

Computations are performed on finite-size computational domains with nonreflecting far-field boundary, conditions. At the inflow boundary, the radiation operator B_1 of Bayliss and Turkel[25] is applied to all of the flow perturbations. This operator may be written in a Cartesian system with the origin located at the source center and with the x coordinate aligned with the freestream direction as

$$B_1 = \frac{1}{c_\infty \beta} \left(1 - \frac{x}{d} \frac{M_\infty}{\beta} \right) \frac{\partial}{\partial t} + \frac{x}{d} \frac{\partial}{\partial x} + \frac{y}{d} \frac{\partial}{\partial y} + \frac{z}{d} \frac{\partial}{\partial z} + \frac{1}{d} \tag{35}$$

where

$$\beta = \sqrt{1 - M_\infty^2}, \qquad d^2 = x^2/\beta^2 + y^2 + z^2 \tag{36}$$

At the outflow boundary, the linearized momentum equations are solved for the velocity perturbations, but the radiation operator B_1 is applied to the pressure perturbation,[26] and the density perturbation is found from

$$\frac{\partial \rho_a}{\partial t} + V_\infty \frac{\partial \rho_a}{\partial x} = \frac{1}{c_\infty^2} \left(\frac{\partial p_a}{\partial t} + V_\infty \frac{\partial p_a}{\partial x} \right) \tag{37}$$

All far-field boundary conditions are transformed to cylindrical-polar coordinates and the same mapping transformations as the interior are applied to them.

D. Spatial Discretization and Time Integration

All of the time-dependent partial differential equations are solved using a high-order explicit time-marching algorithm. The governing equations and the boundary conditions are all put in the semidiscrete form

$$\frac{\mathrm{d}\boldsymbol{Q}}{\mathrm{d}t} + \boldsymbol{R}(\boldsymbol{Q}) = 0 \tag{38}$$

where $\boldsymbol{R}(\boldsymbol{Q})$ represents the discretized residual (collection of the terms involving spatial derivatives and sources) of the governing and boundary condition equations. Residual discretization is carried out using fourth-order, central differences, whereas the time integration is performed using the four-stage Runge–Kutta scheme. Artificial dissipation is added to the residual to augment the scheme against spurious wave developments. A fourth-order, constant coefficient dissipation model was used in all of the computations presented in the paper.

A domain decomposition methodology has been used to parallelize the codes, which scale well on a cluster of Pentium processors.

E. Far-Field Predictions

The Kirchhoff method will be adequate for computing the fore far-field radiation, but it will somewhat lack accuracy for aft far-field radiation because of the shear layer emanating from the shroud. The use of the Ffowcs Williams–Hawkings (FW–H) equation will be more appropriate for aft radiation calculations because it will account for the effects of the flow gradients across the shear layer. However, in the present work, the Kirchhoff method was employed for predicting both fore and aft radiated far-field sound, and the implementation of the FW–H equation will be performed in the future.

The Kirchhoff method employs the Kirchhoff formula given by Farassat and Myers.[27] For a Kirchhoff's surface moving rectilinearly with a Mach vector $\boldsymbol{M}$, this formula is written as

$$4\pi p_a(\boldsymbol{x}, t) = \int\int_S \left[\frac{E_1}{R(1-M_R)} + \frac{p_a E_2}{R^2(1-M_R)}\right]_{\tau^*} \mathrm{d}S \tag{39}$$

where $R = |\boldsymbol{R}|$, $\boldsymbol{R} = \boldsymbol{x} - \boldsymbol{y}(\tau)$, $M_R = \boldsymbol{M}\cdot\boldsymbol{R}/R$, and

$$E_1 = -\boldsymbol{n}\cdot\nabla p_a + (\boldsymbol{M}\cdot\boldsymbol{n})(\boldsymbol{M}\cdot\nabla p_a) + \left[\frac{\cos\varphi - \boldsymbol{M}\cdot\boldsymbol{n}}{c_\infty(1-M_R)} - \frac{\boldsymbol{M}\cdot\boldsymbol{n}}{c_\infty}\right]\frac{\partial p_a}{\partial\tau} \tag{40}$$

$$E_2 = \left[(1-M^2)\big/(1-M_R)^2\right](\cos\varphi - \boldsymbol{M}\cdot\boldsymbol{n}) \tag{41}$$

The Kirchhoff surface emission times τ^* are found by solving the following equation.

$$\tau - t + R(\tau)/c_\infty = 0 \tag{42}$$

Equation (39) is integrated using a forward-time-binning approach. The details of the integration algorithm are found in Ref. 23.

III. Results and Discussion

Fore and aft radiation results for a generic engine are presented in this section. The inlet of the engine has a diameter of 55.9 cm at the fan stage. The inlet hub-to-tip ratio is 0.35, and the exhaust hub-to-tip ratio is 0.51. In the present study, the freestream Mach number and the mass flow through the inlet are taken as 0.2 and 17.8 kg/s, respectively. Along with fore radiation, aft radiation is also investigated, with consideration of a bypass ratio of 4 and a fan compression ratio of 1.1. Based on one-dimensional ideal gas-dynamics relations, these conditions dictate an inlet fan-face Mach number of 0.198 and a throat Mach number of 0.209. The flow Mach number is assumed to remain unchanged across the fan–stator (or exit guide vanes) stage. Based on this assumption and the operating conditions, the mass flow through the exhaust duct is calculated as 14.24 kg/s. These conditions dictate an exhaust fan-face density of 1.002 kg/s. Together with the slight difference in the axial velocity and the difference in density between the outer flow and the exhaust flow, a shear layer emanates from the shroud trailing edge.

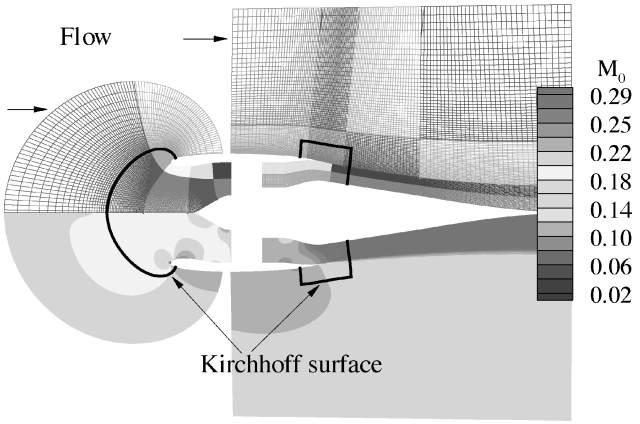

Fig. 2 Generic engine mesh and mean Mach number contours: $M_\infty = 0.2$, $\dot{m} = 17.8$ kg/s, $R_{\mathrm{bp}} = 4.0$, and $R_{\mathrm{fc}} = 1.1$.

A good quality grid with superior orthogonality and smoothness characteristics is critical for aeroacoustic simulations that employ higher-order numerics. The round lip of the engine inlet dictates a wraparound grid topology, which is automatically generated using a conformal mapping procedure.[28] However, the exhaust nacelle has a sharp trailing edge, and consequently, a similar grid is not feasible there. Therefore, the computational mesh shown in Fig. 2 was employed in the study. As is evident from Fig. 2 the inlet and exhaust grids are not connected. Although both grids could be extended to overlap each other and thereby exchange data, this was not done because high-order interpolation schemes would be required, creating extra computational costs and possibly numerical noise. Numerical solutions on the two grids may be carried out separately or simultaneously because they are assigned to different processors in the present parallel computing approach. With an if statement, any desired subblocks of the two grids (inlet and exhaust propagation domains) may easily be switched to the linearized equations or vice versa.

The mean inlet and fan exhaust flowfields computed using the Euler solver are shown in the lower part of Fig. 2. It is clear that a shear layer is emanating from the shroud. Instability waves were observed in the shear layer in long-time computations of the exhaust mean flowfield using the full Euler solver. Therefore, mean flow computations were stopped before these waves appeared. As already mentioned, the far-field boundary conditions are solved for the flow perturbations to the freestream. Because of this and because the inlet and exhaust grids do not communicate data between their respective neighboring outflow and inflow boundaries outside the nacelle, the mean flow contours exhibit slight differences there, as can be clearly seen in the Mach contours in Fig. 2. For the first acoustic case, a combination of the (6, 0) and (6, 1) modes at a frequency of 3120 Hz is considered. At this frequency both modes are cut on into both the inlet and exhaust ducts. The inlet (6, 0) and (6, 1) modes have cutoff ratios of 2.19 and 1.41, respectively, whereas the exhaust (6, 0) and (6, 1) modes have cutoff ratios of 1.89 and 1.26, respectively. The second case considers the (6, 0) mode alone for comparison purposes. In both cases, hard- and soft-wall computations are realized. When the (6, 0) and (6, 1) modes are considered together, their modal shapes are both multiplied by the same reference pressure, but a 45-deg phase difference is introduced between the two. Modal shapes of the inlet and exhaust fan-face sources are shown in Figs. 3 and 4. No phase differences were taken into account in Figs. 3 and 4.

The inlet acoustic field is obtained using the full Euler solver, whereas the exhaust acoustic field is obtained using the linearized

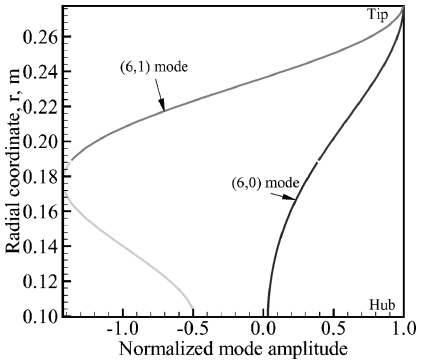

Fig. 3 Inlet fan-face acoustic source modal shape.

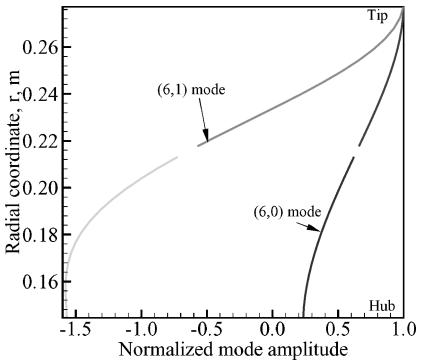

Fig. 4 Exhaust fan-face acoustic source modal shape.

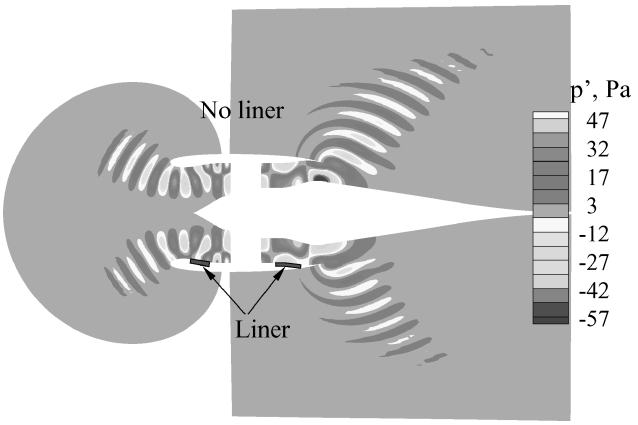

Fig. 5 Acoustic pressure contours; source (6, 0) + (6, 1) modes with 45-deg phase, $M_\infty = 0.2$, $\dot{m} = 17.8$ kg/s, $R_{bp} = 4.0$, $R_{fc} = 1.1$, and 2BPF = 3120 Hz.

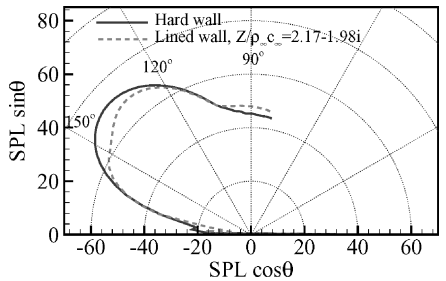

Fig. 6 Forward-arc far-field SPL; source (6, 0) + (6, 1) modes with 45-deg phase difference, $M_\infty = 0.2$, $\dot{m} = 17.8$ kg/s, $R_{bp} = 4.0$, $R_{fc} = 1.1$, and 2BPF = 3120 Hz.

Euler solver. Figure 5 shows the instantaneous acoustic pressure field of the generic engine as generated by the propagation of the (6, 0) and (6, 1) modes, which are cut on at twice the blade passing frequency (BPF), which is 1560 Hz. The upper half of Fig. 5 pertains to the simulation with the hard-wall case and the lower half for simulations with a lined-wall case with a specific impedance value of $Z/\rho_\infty c_\infty = 2.17 - 1.98i$. The liner lengths and locations are shown in Fig. 5. Differences created by the liner in the acoustic field are evident. Forward-arc far-field radiation results shown in Fig. 6 were obtained by Kirchhoff integration on the surface enclosing the inlet mouth as shown in Fig. 2. Figure 7 shows the far-field sound pressure level (SPL) for the exhaust radiation as computed by Kirchhoff integration on the surface enclosing the fan exhaust (Fig. 2). Using the two Kirchhoff surfaces shown in Fig. 2 to compute the far-field sound will not account for the interference effects between the inlet and exhaust acoustic fields. However, computing the far-field noise in this manner is justifiable at this point because no exact information was available on the source modal amplitudes and phases. When this information is available, the interference effects can be taken into account using overlaid grids or a single grid for the two radiation fields and a single Kirchhoff surface. The attenuation effects of the liner are evident in both fore and aft far-field SPL results. Most fore radiation occurred in a direction about 42-deg angle from the inlet axis, whereas most aft radiation occurred in a direction about 38 and 77 deg from the exhaust axis. The latter indicates that two significant lobes occurred for the aft radiation. The one that is closer to the exhaust axis is due to the (6, 0) mode, whereas the other is due to the (6, 1) mode. This will be clearer when we consider only the (6, 0) mode. Total attenuation by the liner was predicted as approximately 3 dB in both the fore and aft peak radiation directions.

The standalone (6, 0) mode was also simulated to see the differences the (6, 1) mode made in the results discussed earlier. Acoustic pressure contours are not shown, but the predicted far-field SPLs are shown in Figs. 8 and 9 for the inlet and exhaust radiation, respectively. It is clear that the fore radiation lobe is now narrower, and in the exhaust radiation pattern there is only one significant lobe, which is at about 35 deg from the exhaust axis. This and the earlier results clearly indicate that the (6, 1) mode radiates to the far field at a higher angle from the engine axis. Again the attenuation effects of the liner are more than evident in the SPL results.

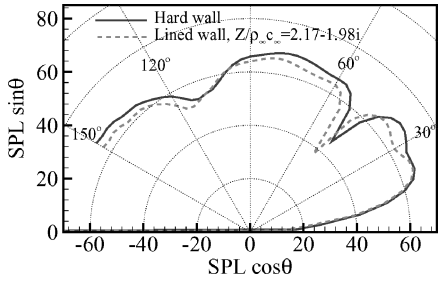

Fig. 7 Aft-arc far-field SPL; source (6, 0) + (6, 1) modes with 45-deg phase difference, $M_\infty = 0.2$, $\dot{m} = 17.8$ kg/s, $R_{bp} = 4.0$, $R_{fc} = 1.1$, and 2BPF = 3120 Hz.

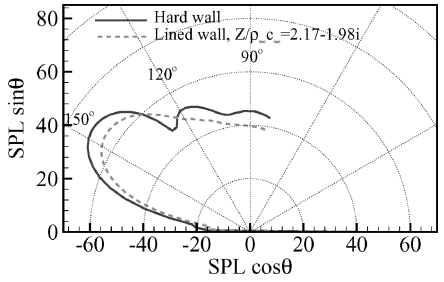

Fig. 8 Forward-arc far-field SPL; source (6, 0) mode, $M_\infty = 0.2$, $\dot{m} = 17.8$ kg/s, $R_{bp} = 4.0$, $R_{fc} = 1.1$, and 2BPF = 3120 Hz.

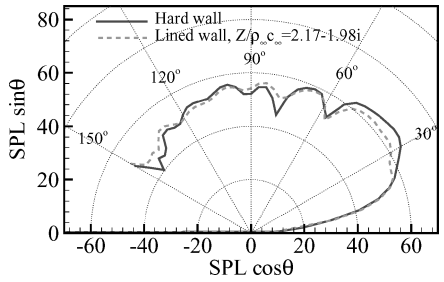

Fig. 9 Aft-arc far-field SPL; source (6, 0) mode, $M_\infty = 0.2$, $\dot{m} = 17.8$ kg/s, $R_{bp} = 4.0$, $R_{fc} = 1.1$, and 2BPF = 3120 Hz.

IV. Conclusions

A general framework for predicting fore and aft acoustic radiation from turbofans has been discussed, and simulations for a generic engine have been carried out. The framework provides for fore radiation being carried out utilizing the full Euler equations and a linearized approach used for the aft radiation analyses. The linearized approach was necessary for the aft radiation problem from the turbofan engine because of difficulties experienced with implementation of the exhaust fan-face boundary conditions and the appearance of inherent shear layer instabilities with the full Euler equations. For the exhaust acoustic calculations, a special form of the characteristics boundary conditions has been used, producing well-behaved results at the inflow boundary with the linearized Euler equations. Fore and aft simulations of acoustic radiation with and without acoustic liners were performed. These simulations were carried out for standalone spinning modes (6, 0) and combinations of modal shapes (6, 0) and (6, 1). Far-field SPLs were computed and analyzed for all cases utilizing the Kirchhoff surface integration methodology. Dominant directions of peak radiation were identified, and attenuation due to the acoustic liner has been predicted in both the fore and aft peak radiation directions.

Acknowledgments

The authors thank L. N. Long and P. J. Morris of the Pennsylvania State University for invaluable discussions.

References

[1]Tyler, J. M., and Sofrin, T. G., "Axial Flow Compressor Noise Studies," *SAE Transactions*, Vol. 70, 1962, pp. 309–332.

[2]Rumsey, C. L., Biedron, R. T., Farassat, F., and Spence, P. L., "Ducted-Fan Engine Acoustic Predictions Using a Navier–Stokes Code," *Journal of Sound and Vibration*, Vol. 213, No. 4, 1998, pp. 643–664.

[3]Nayfeh, A. H., Kaiser, J. E., and Telionis, D. P., "Acoustics of Aircraft Engine–Duct Systems," *AIAA Journal*, Vol. 13, No. 2, 1975, pp. 130–153.

[4]Nallasamy, M., Sutliff, D. L., and Heidelberg, L. J., "Propagation of Spinning Acoustic Modes in Turbofan Exhaust Ducts," *Journal of Propulsion and Power*, Vol. 16, No. 5, 2000, pp. 736–743.

[5]Parrott, T. L., and Jones, M. G., "Parallel-Element Linear Impedances for Improved Absorption of Broadband Sound in Ducts," *Noise Control Engineering Journal*, Vol. 43, No. 6, 1995, pp. 183–195.

[6]Spence, P. L., "Ducted Fan Noise Prediction Using Wave Envelope Analysis and the Kirchhoff Formula," *Proceedings of the 3th AIAA/CEAS Aeroacoustics Conference*, AIAA Reston, VA, 1997, pp. 539–549.

[7]Shim, I. B., Kim, J. W., and Lee, D. J., "Numerical Study on Radiation of Multiple Pure Tone Noise from an Aircraft Engine Inlet," AIAA Paper 99-1831, May 1999.

[8]Astley, R. J., and Eversman, W., "Wave Envelope and Infinite Element Schemes for Fan Noise Radiation from Turbofan Inlets," *AIAA Journal*, Vol. 22, No. 12, 1984, pp. 1719–1726.

[9]Eversman, W., Parrett, A. V., Preisser, J. S., and Silcox, R. J., "Contributions to the Finite Element Solution of the Fan Noise Radiation Problem," *Journal of Vibration, Acoustics, Stress and Reliability in Design*, Vol. 107, No. 2, 1985, pp. 216–223.

[10]Myers, M. K., "Boundary Integral Formulations for Ducted Fan Radiation Calculations. Confederation of European Aerospace Societies, CEAS/AIAA Paper 95-076, June 1995.

[11]Stanescu, D., Ait-Ali-Yahia, D., Habashi, W. G., and Robichaud, M. P., "Multidomain Spectral Computations of Sound Radiation from Ducted Fans," *AIAA Journal*, Vol. 37, No. 3, 1999, pp. 296–302.

[12]Özyörük, Y., and Long, L. N., "A New Efficient Algorithm for Computational Aeroacoustics on Parallel Processors," *Journal of Computational Physics*, Vol. 125, No. 1, 1996, pp. 135–149.

[13]Ahuja, V., Özyörük, Y., and Long, L. N., "Computational Simulations of Fore and Aft Radiation From Ducted Fans," AIAA Paper 2000-1943, June 2000.

[14]Thompson, K. W., "Time-Dependent Boundary Conditions for Hyperbolic Systems," *Journal of Computational Physics*, Vol. 68, No. 1, 1987, pp. 1–24.

[15]Thompson, K. W., "Time-Dependent Boundary Conditions for Hyperbolic Systems, II," *Journal of Computational Physics*, Vol. 89, No. 2, 1990, pp. 439–461.

[16]Giles, M. B., "Non-reflecting Boundary Conditions for the Euler Equations," Computational Fluid Dynamics Lab., MA, Rept. TR 88-1, Massachusetts Inst. of Technology, Cambridge, MA, Feb. 1988.

[17]Richards, S., Zhang, X., Chan, X. X., and Nelson, P. A., "The Evaluation of Non-reflecting Boundary Conditions for Duct Acoustic Computation," *Journal of Sound and Vibration*, Vol. 270, No. 3, 2004, pp. 539–557.

[18]Hu, F. Q., "A Stable, Perfectly Matched Layer for Linearized Euler Equations in Unsplit Physical Variables," *Journal of Computational Physics*, Vol. 173, No. 2, 2001, pp. 455–480.

[19]Özyörük, Y., Ahuja, V., and Long, L. N., "On Numerical Simulations of Fore and Aft Noise Radiation from Turbofans," AIAA Paper 2003-0540, Jan. 2003.

[20]Agarwal, A., Morris, P. J., and Mani, R., "Calculation of Sound Propagation in Nonuniform Flows: Suppression of Instability Waves," *AIAA Journal*, Vol. 42, No. 1, 2004, pp. 80–88.

[21]Özyörük, Y., Long, L. N., and Jones, M. G., "Time-Domain Numerical Simulation of a Flow-Impedance Tube," *Journal of Computational Physics*, Vol. 146, No. 1, 1998, pp. 29–57.

[22]Özyörük, Y., "Parallel Computation of Forward Radiated Noise of Ducted Fans Including Acoustic Treatment," *AIAA Journal*, Vol. 40, No. 3, 2002, pp. 450–455.

[23]Özyörük, Y., and Long, L. N., "Computation of Sound Radiating from Engine Inlets," *AIAA Journal*, Vol. 35, No. 5, 1996, pp. 894–901.

[24]Myers, M. K., "On the Acoustic Boundary Condition in the Presence of Flow," *Journal of Sound and Vibration*, Vol. 71, No. 3, 1980, pp. 429–434.

[25]Bayliss, A., and Turkel, E., "Far Field Boundary Conditions for Compressible Flow," *Journal of Computational Physics*, Vol. 48, No. 2, 1982, pp. 182–199.

[26]Tam, C. K. W., and Webb, J. C., "Dispersion-Relation-Preserving Finite Difference Schemes for Computational Acoustics," *Journal of Computational Physics*, Vol. 107, No. 2, 1993, pp. 262–281.

[27]Farassat, F., and Myers, M. K., "Extension of Kirchhoff's formula for Radiation from Moving Surfaces," *Journal of Sound and Vibration*, Vol. 123, No. 3, 1988, pp. 451–460.

[28]Özyörük, Y., "Sound Radiation From Ducted Fans Using Computational Aeroacoustics On Parallel Computers," Ph.D. Dissertation, Dept. of Aerospace Engineering, Pennsylvania State Univ., University Park, PA, Dec. 1995.

H. M. Atassi
Associate Editor